AGU PUBLICATIONS

JGR

Journal of Geophysical Research: Atmospheres

RESEARCH ARTICLE
10.1002/2015JD024012

Key Points:
- The formaldehyde column depends on the concentrations of OH radical and volatile organic compounds
- Top-down constraints of volatile organic compound emissions should consider variations of OH radical
- The influence of nitrogen oxides on the formaldehyde column includes its feedback on OH radical concentrations

Correspondence to:
L. C. Valin,
lcvalin@ldeo.columbia.edu

Citation:
Valin, L. C., A. M. Fiore, K. Chance, and G. González Abad (2016), The role of OH production in interpreting the variability of CH_2O columns in the southeast U.S., *J. Geophys. Res. Atmos., 121*, 478–493, doi:10.1002/2015JD024012.

Received 29 JUL 2015
Accepted 20 NOV 2015
Accepted article online 24 NOV 2015
Published online 7 JAN 2016

The role of OH production in interpreting the variability of CH_2O columns in the southeast U.S.

L. C. Valin[1], A. M. Fiore[1,2], K. Chance[3], and G. González Abad[3]

[1]Lamont Doherty Earth Observatory, Columbia University, Palisades, New York, USA, [2]Department of Earth and Environmental Studies, Columbia University, Palisades, New York, USA, [3]Harvard Smithsonian Center for Astrophysics, Harvard University, Cambridge, Massachusetts, USA

Abstract Formaldehyde (CH_2O), a key atmospheric oxidation intermediate that is detectable from satellite-based UV/visible spectrometers, is primarily formed when hydroxyl radical (OH) reacts with volatile organic compounds (VOC) and is removed by photolysis, reaction with OH or deposition. We investigate the influence of OH and VOC variability on the CH_2O column using a steady state model and the WRF-Chem regional chemical transport model over the southeast United States for the summer of 2012 (June–August). The steady state model indicates that the CH_2O column primarily depends on OH production rates (P_{OH}) at low concentrations of OH ($<3\times10^6$ molecules cm^{-3}), on both P_{OH} and VOC reactivity (VOCR: $\Sigma_i k_i[VOC]_i$) at moderate concentrations of OH (3×10^6–7×10^6 molecules cm^{-3}) and on VOCR at high concentrations of OH ($>7\times10^6$ molecules cm^{-3}). When constrained with WRF-Chem values of boundary layer average P_{OH} and VOCR, the steady state model of CH_2O explains most of the daily ($r^2=0.93$) and average June–August ($r^2=0.97$) spatial variance of the fully simulated cloud-free CH_2O column. These findings imply that measurements of the CH_2O column offer the potential to better understand the processes affecting oxidation, particularly in remote regions, where OH concentrations are low. The findings also suggest that the inference of VOC emissions based on measurements of CH_2O, or any other intermediate oxidation species with a photolytic lifetime that is short relative to removal by reaction with OH (e.g., glyoxal), should carefully account for the influence of OH on the observed pattern, especially where OH concentrations are below 5×10^6 molecules cm^{-3}, as occurs in remote forests, where OH strongly varies, as occurs downwind of large nitrogen oxide (NO_x: NO+NO_2) emission sources, or where OH sources are potentially biased.

1. Introduction

The hydroxyl radical (OH) is the most important oxidant in the troposphere, involved in the production of O_3 and particulate matter, and the removal of several greenhouse gases (e.g., CH_4 and HCFCs). Some fraction of reactions between OH and volatile organic compounds (VOC) leads to the formation of formaldehyde (CH_2O). As the next generation of space-based UV/visible sensors capable of observing CH_2O undergoes development [*Chance et al.*, 2013; *Fishman et al.*, 2012], there is a need and opportunity to better understand the relationship of the CH_2O column with OH and its VOC precursors, such as methane and isoprene.

Remotely sensed UV-visible measurements offer the potential to routinely measure the spatial distribution of CH_2O [e.g., *De Smedt et al.*, 2012; *González Abad et al.*, 2015]. Measurements from space-based spectrometers have provided extensive detail on the variability of the CH_2O column on daily [e.g., *Palmer et al.*, 2006], seasonal [e.g., *Martin et al.*, 2004; *Palmer et al.*, 2006; *Fu et al.*, 2007] and interannual time scales [e.g., *Abbot et al.*, 2003; *De Smedt et al.*, 2010] at global [e.g., *Stavrakou et al.*, 2009a, 2009b; *Fortems-Cheiney et al.*, 2012], regional [e.g., *Fu et al.*, 2007; *Millet et al.*, 2008; *Dufour et al.*, 2009; *Marais et al.*, 2012; *Barkley et al.*, 2013; *Jin and Holloway*, 2015], and urban spatial scales [e.g., *Duncan et al.*, 2010; *Boeke et al.*, 2011; *Witte et al.*, 2011; *Zhu et al.*, 2014]. The measurements of the CH_2O column have primarily been used to investigate the emissions of isoprene (E_{ISOP}) and other short-lived VOC that give rise to large, localized enhancements of CH_2O [e.g., *Palmer et al.*, 2003, 2006; *Fu et al.*, 2007; *Barkley et al.*, 2008, 2013; *Millet et al.*, 2008; *Stavrakou et al.*, 2009a, 2009b; *Curci et al.*, 2010; *Marais et al.*, 2012, 2014; *Zhu et al.*, 2014]. It is well known, however, that the concentration of CH_2O also depends on the concentration of OH, both in isoprene-rich regions [e.g., *Sumner et al.*, 2001; *Butler et al.*, 2008; *Galloway et al.*, 2012] and in regions where CH_4 is the dominant VOC [e.g., *Song et al.*, 2010]. We thus hypothesize that variability in the CH_2O column systematically reflects variations of the OH radical, in addition to reflecting variations of VOC.

To investigate this hypothesis, we first formulate a steady state equation for the CH_2O column (section 2). We then test the assumptions underlying this steady state model using the WRF-Chem regional model (section 3) before discussing the implications for inferring E_{ISOP} from CH_2O column measurements (section 4). We also explore the potential for daily CH_2O column measurements (section 5) to provide constraints on the production of OH radicals (P_{OH}) and describe the necessary conditions for such constraints (section 6) before concluding (section 7).

2. A Steady State Model for the CH_2O Column: *f*(P_{OH},VOC Reactivity)

The dominant source of CH_2O is the reaction of OH with VOC, primarily CH_4, isoprene or one of their products, with small contributions from ozonolysis and photolysis [*Fortems-Cheiney et al*., 2012]. In contrast, the CH_2O lifetime depends less on the concentration of OH as it is determined both by photolysis ($J_{CH2O} \approx 0.3\ h^{-1}$; typical of summertime northern midlatitudes) and by reaction with OH ($0.3\ h^{-1}$ at $[OH] = 1 \times 10^7$), with much slower loss to deposition. As a result, the concentration of CH_2O depends on the concentration of OH, both in "background" conditions where most OH reacts with CH_4 or CO [e.g., *Song et al*., 2010] and in isoprene-rich conditions [e.g., *Butler et al*., 2008; *Galloway et al*., 2012].

To isolate the influence of OH production (P_{OH}) on the CH_2O column, we write both CH_2O sources and sinks in terms of P_{OH}. P_{OH} accounts for all primary (e.g., $O^1D + H_2O$) and secondary (e.g., $NO + HO_2$) sources of OH. At steady state, OH production and OH loss are equal (i.e., $P_{OH} = \Sigma k_{Xi+OH}[X_i][OH]$). The rate of CH_2O production can be related to the rate of OH loss by incorporating the fractional yield of CH_2O (α_{Xi}) from each reaction that consumes OH ($P_{CH2O} = \Sigma\ \alpha_{Xi}\, k_{Xi+OH}\, [X_i]\, [OH]$). Instead of treating each species and its yield separately [e.g., $\alpha_{CH4} \leq 1$, $\alpha_{CO,NO2} = 0$; e.g., *Sumner et al*., 2001; *Galloway et al*., 2012], we define an effective yield (α_{eff}: $P_{CH2O}\, P_{OH}^{-1}$). Thus, the rate of CH_2O production equals the rate of OH production (P_{OH}) multiplied by the effective yield of CH_2O (α_{eff}: $P_{CH2O}\, P_{OH}^{-1}$). We evaluate this approach by quantifying α_{eff} in WRF-Chem (section 3.3) considering both the impacts of individual RO_2 radical pathways on α_{eff} (section 3.3.1) and the impacts of VOC composition (section 3.4). The CH_2O loss rate equals the rate of its loss by photolysis (J_{CH2O}) plus its loss by reaction with OH ($k_{CH2O+OH}[OH]$). The concentration of OH equals its source (P_{OH}) divided by it sink, which we assume is dominated by the reactivity weighted concentration of VOC (VOCR:$\Sigma_i k_i[VOC_i] + k_{CO+OH}[CO]$).

At midday, CH_2O sources and sinks are both maximum and the CH_2O lifetime is sufficiently short to assume that the CH_2O concentration is in steady state. Assuming that alkene ozonolysis and photolysis are negligible sources of CH_2O, we write a steady state equation for the CH_2O concentration as

$$[CH_2O]_{steady\ state} = \frac{\alpha_{eff} P_{OH}}{(J_{CH2O} + k_{CH2O+OH} P_{OH}/VOCR)} \quad (1)$$

At high OH concentrations (i.e., high P_{OH} or low VOCR), loss by reaction with OH is dominant and the concentration of CH_2O depends on VOCR ($\sim\alpha_{eff}$ VOCR/$k_{CH2O+OH}$). At low OH concentrations (i.e., low P_{OH} or high VOCR), loss by photolysis is dominant and the concentration of CH_2O depends on P_{OH} ($\sim\alpha_{eff}$ P_{OH}/J_{CH2O}). For a given isoprene emission rate, the feedback of P_{OH} on VOCR must also be considered because VOCR decreases as P_{OH} increases. The precise magnitude of this decrease is uncertain and mechanism dependent [e.g., *Karl et al*., 2009, *Fuchs et al*., 2013; *Nolscher et al*., 2014]. We quantify this effect in section 3.3.2 using WRF-Chem and find that the feedbacks of P_{OH} on CH_2O removal (i.e., via both P_{OH} and VOCR; equation (1), denominator) do not offset the impact of P_{OH} on CH_2O production (equation (1), numerator).

Figure 1 shows steady state CH_2O columns (contours) computed as a function of P_{OH} (*x* axis) and VOCR (*y* axis) where we specify values for the effective yield ($\alpha_{eff} = 0.30\, P_{CH2O}\, P_{OH}^{-1}$) and the loss rate constants ($J_{CH2O} = 0.3\ h^{-1}$; $k_{CH2O+OH} = 0.\ 3 \times 10^{-7}\ cm^3\ molecule^{-1}\ h^{-1}$). To convert steady state CH_2O concentrations to column values, we assume that VOCR and P_{OH} are well mixed below 2 km. Above 2 km, CH_2O photolysis is fast, VOCR is low, and P_{OH} is low, thus resulting in a small contribution to the total CH_2O column, which we assume here to be a constant value (2×10^{15} molecules cm^{-2}). Where the concentration of OH is low ($P_{OH}/VOCR < 3 \times 10^6$ molecules cm^{-3}; Figure 1) and photolysis is dominant, the CH_2O column is more

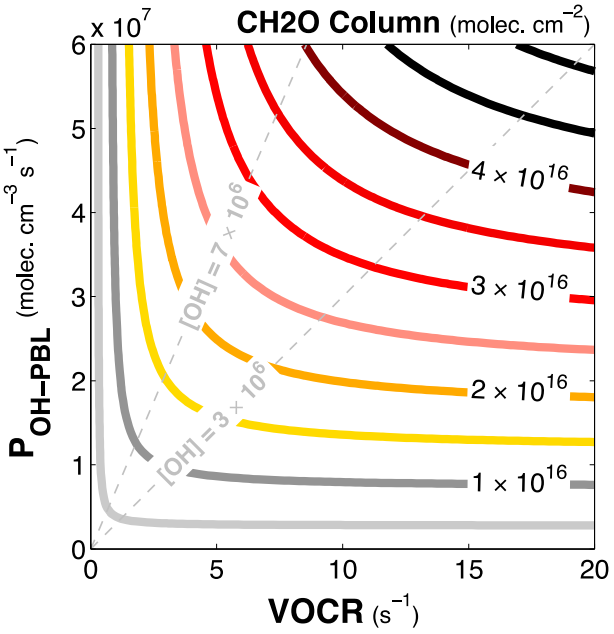

Figure 1. The steady state CH_2O column (colored curves; molecules cm^{-2}) as a function of VOC reactivity (*x* axis; VOCR; s^{-1}) and OH production (*y* axis; P_{OH}; molecules cm^{-3} s^{-1}). The column is computed using equation (1) ($\alpha_{eff} = 0.3\ P_{CH2O}\ P_{OH}^{-1}$, $J_{CH2O} = 0.30\ h^{-1}$, $k_{CH2O+OH}[OH] = 0.03\ h^{-1}$ at $[OH] = 1 \times 10^6$ molecules cm^{-3}) assuming that P_{OH} and VOCR are uniformly mixed from 0 to 2 km above ground level and are zero above 2 km. Values of constant OH concentration are indicated on the plot (gray dashed lines) under the assumption that VOCR is the only sink of OH radicals.

sensitive to changes of P_{OH} and less sensitive changes in VOCR. The opposite is true when the OH concentration is high (P_{OH}/VOCR $> 7 \times 10^6$ molecules cm^{-3}; Figure 1). At OH concentrations in between these end member cases, the CH_2O column is sensitive to both P_{OH} and VOCR. For a constant OH concentration, the sensitivity (slope) of the CH_2O column to a perturbation of VOCR is steep for high OH concentrations (e.g., a steep increase of CH_2O column contours following along the $[OH] = 7 \times 10^6$ molecules cm^{-3} gray line; Figure 1) and is shallow for low OH concentrations (e.g., a shallow increase along the $[OH] = 3 \times 10^6$ molecules cm^{-3}; gray line; Figure 1).

3. Testing the Steady State Model With the Regional WRF-Chem Model

3.1. Model Configuration

We now investigate the relationship of P_{OH} and VOCR to the CH_2O column using WRF-Chem, a state-of-the-art regional climate chemistry model [*Grell et al.*, 2005]. We simulate the chemistry over the southeast United States (27.7°N–43.8°N; 74.7°W–101.3°W) at 36 km horizontal grid resolution (50 N-S × 70 E-W) for 21 May 2012–31 August 2012. The model has 35 terrain-following hybrid pressure levels varying from ~85 m thickness in the first model level to 300 m thickness in the layer 2.5 km above ground level and 3000 m thickness at the model top ($z \approx 21$ km AGL). We analyze daily 1 P.M. CST model results for June – August 2012 and discard the five outermost grid rows of the domain to avoid excessive influence from the boundary conditions.

The chemical mechanism builds on the RACM2 photooxidation mechanism [*Goliff et al.*, 2013] with recent updates to the isoprene oxidation pathways and extended monoterpene and monoterpene nitrate chemistry [*Browne et al.*, 2014]. The updates to isoprene photochemistry follow those described by *Paulot et al.* [2009a, 2009b], with further updates to peroxy radical isomerization rates [*Crounse et al.*, 2011, 2012] and product yields [*Peeters and Muller*, 2010]. In addition to standard model diagnostics, we track the rates of different classes of reactions within the mechanism to quantify the processes controlling the production and loss of OH, RO_2, and CH_2O.

We use ERA-interim reanalysis [*Dee et al.*, 2011] as initial and boundary conditions for meteorological conditions (6-hourly), and MOZART-4/GEOS-5 output for chemical boundary conditions (6-hourly; *Emmons et al.*, 2010; http://www.acd.ucar.edu/wrf-chem/mozart.shtml). For emissions, we use the 2005 U.S. National Emission Inventory (NEI2005, available online ftp://aftp.fsl.noaa.gov/divisions/taq/emissions_data_2005/). The anthropogenic nitrogen oxide (NO_x: $NO + NO_2$) emission rate (E_{NOx}) integrated over the domain is 3.65 Tg N y^{-1}. We also perform a sensitivity simulation in which we uniformly decrease anthropogenic E_{NOx} by a factor of 10. There are no biomass burning or lightning emission sources included in the simulation and any aircraft emissions included in the NEI2005 are allocated to the lower model layers. Biogenic emissions are driven by MEGAN v2.04 [*Guenther et al.*, 2006] (http://www.acd.ucar.edu/wrf-chem/download.shtml). Domain total June–August 2012 biogenic E_{NOx} is 0.31 Tg N y^{-1}, and E_{ISOP} is 32 Tg C y^{-1}. The emission rate for isoprene is in line with previous analyses [e.g., *Millet et al.*, 2008] given differences in domain size and interannual variability.

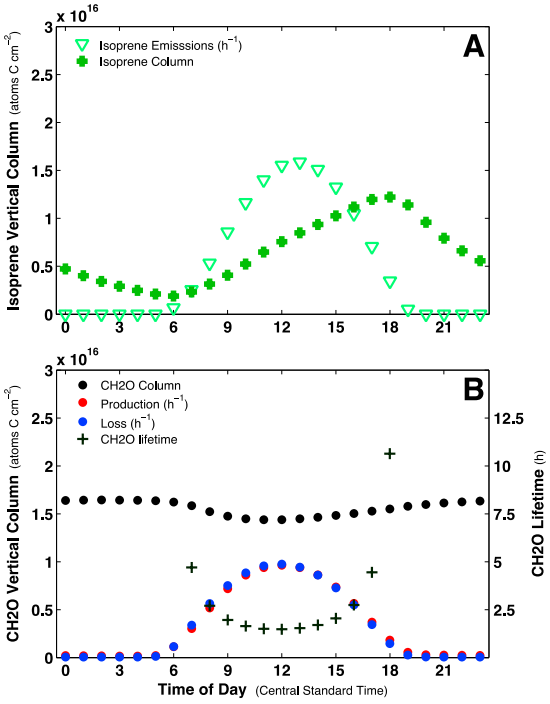

Figure 2. The diurnal profile of (a) isoprene emissions (atom C cm^{-2} h^{-1}) and the isoprene column (atom C cm^{-2}) and (b) the CH_2O vertical column (atom C cm^{-2}) and the column integrated production rate (atom C cm^{-2} h^{-1}), loss rate (atom C cm^{-2} h^{-1}) and lifetime of CH_2O (h) for June–August 2012 over the southeast U.S. (32°N–38°N; 75°W–90°W), following the approach of *Millet et al.* [2008].

3.2. Analysis of CH_2O Column Variability and its Drivers

3.2.1. Diurnal Variability of the CH_2O Column and the Isoprene Columns

At a regional scale (32°N–38°N; 75°W–90°W), the CH_2O column is near steady state throughout the day (Figure 2b), supporting our approach to understand CH_2O variability (section 2). The column integrated sources and sinks of CH_2O are nearly identical except for a small offset in their rise through early morning and their fall in late afternoon, and a small difference through the nighttime due to production via reactions of O_3, NO_3, and OH with VOC (Figure 2b). At a typical wind speed of 5 m s^{-1}, the lifetime of CH_2O at midday (~2 h) corresponds to 36 km, or one model grid cell in our simulation. Thus, it is reasonable to assume that the CH_2O column at 1 P.M. (post meridiem) reflects the balance of local sources and sinks.

While the steady state approximation for the CH_2O column is justified (Figure 2b), column integrated isoprene, a major CH_2O precursor, is not in steady state with its emissions (Figure 2a). The diurnal pattern of isoprene emissions is largest at midday and near zero at nighttime (Figure 2a). The isoprene column increases through the daytime, as emissions exceed removal, and then decreases through the night with an *e*-folding timescale of 5.5 h due to chemical loss (i.e., O_3, OH, and NO_3) and transport out of the region, in agreement with previous results [*Millet et al.*, 2008]. The increase of the isoprene column through midday, at a rate of 2×10^{15} atom C cm^{-2} h^{-1} or 8% of the emission rate at noon, indicates that P_{OH} is insufficient to oxidize all available isoprene, let alone its oxidation products to CH_2O. Thus, we conclude that isoprene is not in steady state with its emissions.

3.2.2. Spatial Variability of the CH_2O Column

We next explore the spatial patterns of summer average E_{ISOP}, VOCR, P_{OH} and the steady state estimate of the CH_2O column at 1 P.M. CST (Figure 3, left column). Unless otherwise stated, we compute the steady state value of the CH_2O column using simulated PBL-average (< 2.5 km) values for P_{OH} and VOCR as inputs to equation (1), and we specify the yield of CH_2O per OH consumed ($\alpha_{eff} = 0.30\, P_{CH2O}\, P_{OH}^{-1}$) and loss rate constants ($J_{CH2O} = 0.3\ h^{-1}$; $k_{CH2O+OH} = 0.3 \times 10^{-7}$ molecules^{-1} cm^3 h^{-1}). We convert the PBL steady state value to a column value in all grid cells using the slope (3.1×10^5 cm) and *y* intercept (2×10^{15} molecules cm^{-2}) derived from the reduced major axis linear regression of the fully simulated CH_2O column to the PBL average CH_2O concentration for all daily 1 P.M. CST cloud-free WRF-Chem grid cells over land ($r^2 = 0.98$; N = 106,320). The strong correlation supports our assumption that CH_2O concentrations below 2.5 km drive the overall variability of the column, with a smaller and more uniform contribution above 2.5 km.

The June–August 2012 average spatial pattern of isoprene emissions is highly variable, with a maximum over the Ozarks (35°N–38°N; 91°W–95°W) where emissions exceed all other high-emitting regions by 50%–100% (Figure 3a) [e.g., *Wiedinmyer et al.*, 2005; *Carlton and Baker*, 2011]. The spatial pattern of VOCR closely resembles the pattern of E_{ISOP} with slight smoothing due to transport ($r^2 = 0.90$; Figure 3a versus 3d), indicating the importance of isoprene emission to total VOCR during summer in the region [e.g., *Millet et al.*, 2008]. On average, P_{OH} is relatively uniform at a regional scale except for local maxima over large NO_x emission sources where $NO + HO_2$ reactions strongly enhance P_{OH} (Figure 3g). According to Figure 1, at P_{OH} of 2.5×10^7 molecules cm^{-3} s^{-1} (i.e., the regional background value; Figure 3g), the CH_2O column will linearly

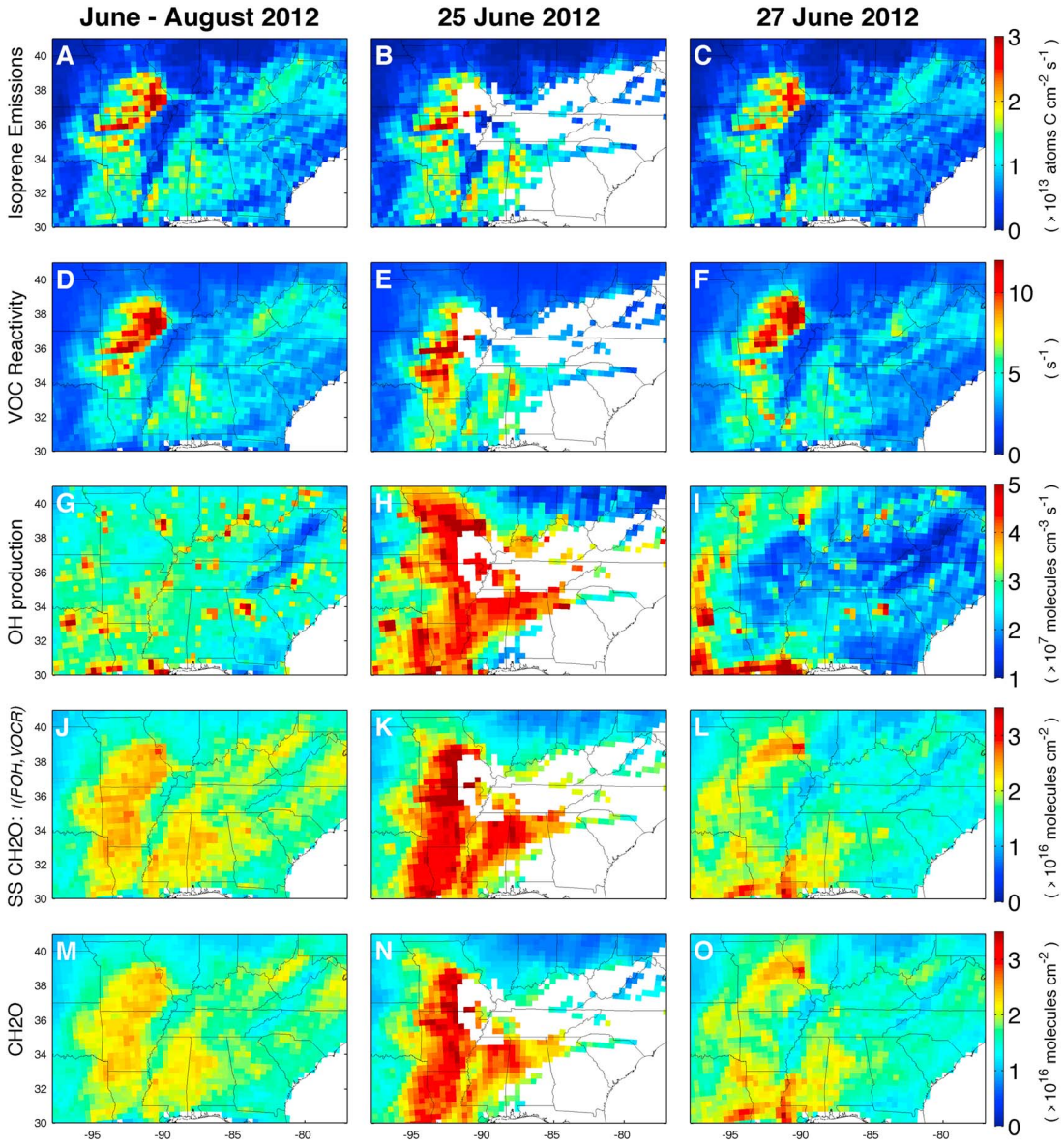

Figure 3. WRF-Chem 19 UTC (1 P.M. Central Standard Time; CST) (a–c) E_{ISOP} (atoms C cm^{-2} s^{-1}), (d–f) PBL VOCR ($z = 0$–2.5 km; s^{-1}), (g–i) P_{OH} ($z = 0$–2.5 km; molecules cm^{-3} s^{-1}) and the (j–l) steady state CH_2O column (molecules cm^{-2}; equation (1); see text), and the (m–o) fully simulated CH_2O column (molecules cm^{-2}) for the June–August 2012 average (left column), 25 June (middle column) and 27 June 2012 (right column). Only values from cloud-free grid cells over land are included in the results.

respond to VOCR and by extension to E_{ISOP} for VOCR less than ~5 s^{-1} but will saturate at larger values of VOCR (i.e., $P_{OH}/VOCR \leq 5 \times 10^6$ molecules cm^{-3}). The corresponding threshold where the CH_2O column will saturate with respect to increases in E_{ISOP} is ~1×10^{13} atom C cm^{-2} s^{-1} (Figures 3a and 3d). Approximately 25% of the grid cells over land are above this threshold and contribute 54% of the total E_{ISOP}.

Thus, the spatial pattern of the June–August average CH_2O column is described well by a reduced major axis linear regression to E_{ISOP} (Figures 3a versus 3m, $r^2 = 0.62$) and VOCR (Figures 3d versus 3m, $r^2 = 0.69$) where E_{ISOP} is less than 1×10^{13} atom C cm^{-2} s^{-1} ($N = 1569$ grid cells) but saturates at ~2.5×10^{16} molecules cm^{-2} for larger values of E_{ISOP} (Figures 3a versus 3m). As a result, E_{ISOP} and VOCR explain less spatial variance of the CH_2O column where E_{ISOP} is greater than 1×10^{13} atom C cm^{-2} s^{-1} ($N = 577$ grid cells; $r^2 = 0.40$, 0.34, respectively). The steady state model, which accounts for these saturating effects by considering variations of P_{OH} (Figure 1), explains nearly all of the spatial variance in the CH_2O columns ($r^2 = 0.97$; Figures 3j versus 3m),

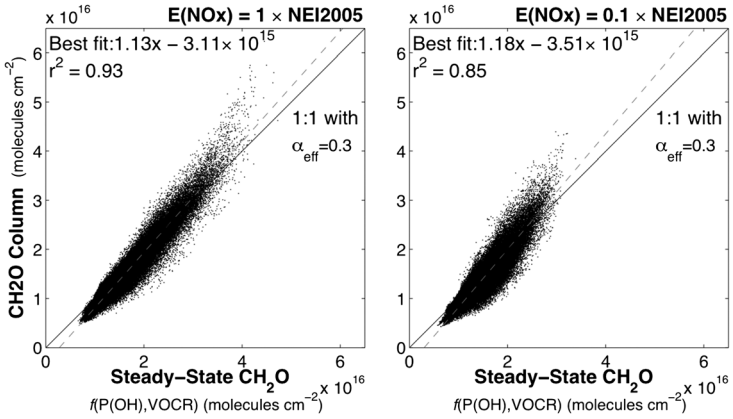

Figure 4. The daily 1 P.M. CST June–August 2012 CH_2O column (*y* axis; molecules cm^{-2}) versus the steady state CH_2O column (*x* axis; molecules cm^{-2}; equation (1)) for all cloud-free grid cells over land in the (a) standard simulation ($E_{NOx} = 1 \times$ NEI2005) and (b) in a simulation with E_{NOx} reduced tenfold ($E_{NOx} = 0.1 \times$ NEI2005). The reduced major axis regression (dashed) and one-to-one (solid) line are included.

including where E_{ISOP} is large ($>1 \times 10^{13}$ atom C cm^{-2} s^{-1}; $r^2 = 0.93$). The threshold at which the CH_2O column saturates with respect to increases of VOCR, or to E_{ISOP} by extension, depends on the background average P_{OH} (Figure 1). Thus, biases of P_{OH} [e.g., *Lelieveld et al.*, 2008; *Butler et al.*, 2008] or failure to accurately segregate isoprene from OH sources [e.g., *Butler et al.*, 2008] will impact the simulated relationship of the CH_2O column to E_{ISOP}, especially in high-VOC, low-P_{OH} conditions (Figure 1, lower right corner).

3.3. The Sensitivity of the CH_2O Column to E_{NOx}

Due to the implementation of successful and ongoing NO_x emission control strategies, NO_2 columns decreased by ~30% over U.S. cities from 2005 to 2011 [*Russell et al.*, 2012] and by 30–40% over the east U.S. from 2005 to 2013 [*Lamsal et al.*, 2015]. NO_x is a major source of OH (i.e., NO-HO_2 reactions, O_3 production) and thus we expect variations of E_{NOX} to affect the CH_2O column. The concentration of NO_x also affects the rates of the high-yield RO_2-NO reactions relative to the lower yield RO_2-HO_2 reactions and thus should affect α_{eff} [e.g., *Palmer et al.*, 2003; *Millet et al.*, 2008; *Marais et al.*, 2012]. To disentangle the influences of NO_x on α_{eff} (section 3.3.1) and P_{OH} (section 3.3.2), we perform a WRF-Chem simulation identical to our base case except we decrease anthropogenic E_{NOx} by a factor of 10. We evaluate the role of individual reaction pathways (i.e., α_{eff}) leading to CH_2O production in both simulations (Figures 4–7 and Table 1).

3.3.1. Dependence of the CH_2O Yield From RO_2 Chemistry on E_{NOx}

Until now we have assumed that α_{eff} ($0.3\ P_{CH2O}\ P_{OH}^{-1}$) and J_{CH2O} ($0.3\ h^{-1}$) are constant. The production of CH_2O from RO_2 radicals (i.e., α_{eff}), however, is expected to depend on the relative concentrations of HO_2, RO_2 and NO and on the identity of the parent VOC (e.g., CH_4 or isoprene). Our initial findings suggest that in the southeast U.S. these effects are small; the quality of the linear fit of the fully simulated CH_2O column to the steady state model (Figure 3) suggests that any variability in α_{eff} resulting from the details of the RO_2 radical chemistry is small relative to the variability driven by P_{OH} or VOCR. Furthermore, for a tenfold decrease of anthropogenic E_{NOx}, we find that there is little change in the slope of the fully simulated CH_2O column to the steady state estimate of the column assuming the same α_{eff} in both regressions (Figures 4a versus 4b).

The initial finding that α_{eff} does not depend strongly on E_{NOx} motivates us to investigate the parameters affecting α_{eff} in more detail. Table 1 reports all known processes affecting α_{eff} in WRF-Chem. Instantaneous rates and yields are calculated explicitly at 1 P.M. CST in WRF-Chem for three locations, each with different photochemical characteristics: a high-isoprene, low-NO_x regime (the Ozarks; 37°N, 92°W); a high-isoprene, high-NO_x regime (Atlanta; 34°N, 84°W); and a low-isoprene, low-NO_x regime (central Illinois; 40°N, 89°W).

The results presented in Table 1 confirm previous findings: RO_2-NO reactions are high yield and RO_2-HO_2 reactions are low yield; these reactions together determine the fate of ~75–95% of all RO_2 [e.g., *Archibald et al.*, 2010, and references therein; *Marais et al.*, 2012; *Mao et al.*, 2013]. Thus, we expect that α_{eff} should be larger

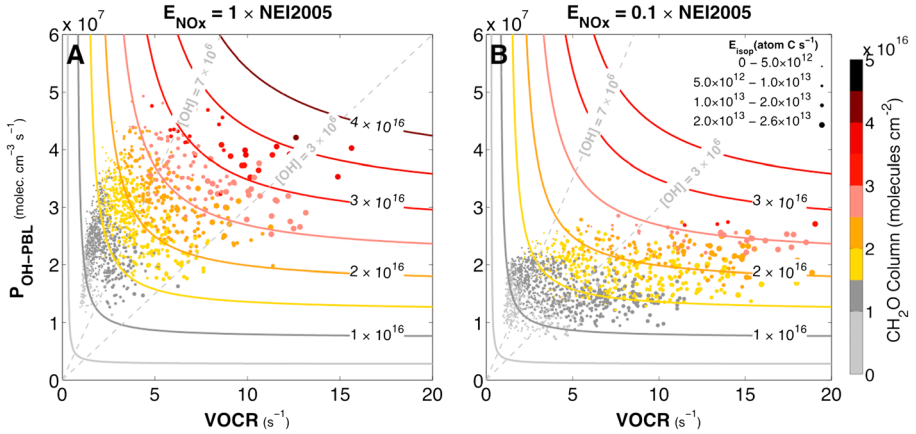

Figure 5. Daily June–August 2012 1 P.M. CST CH_2O column (colors; molecules cm^{-2}) for boundary layer (≤2.5 km) average P_{OH} (*y* axis; molecules cm^{-3} s^{-1}) and VOCR (*x* axis; s^{-1}) in WRF-Chem grid cells over land (36 km × 36 km) that have been averaged to a spatial scale of 216 km × 216 km for (a) the standard simulation and for (b) the sensitivity simulation in which anthropogenic E_{NOx} is decreased by a factor of 10. The magnitude of E_{ISOP} in each grid cell is indicated by the size of the marker. E_{ISOP} is identical in the two simulations, but on average, there is 51% more VOCR per unit of E_{ISOP} in the lower E_{NOx} scenario due to the decrease of P_{OH}. We include only values where fewer than 20% of the native 36 km × 36 km grid cells in the spatial average had clouds. Contours from Figure 1 are included for reference.

in the high-E_{NOx} simulation. However, ~5–25% of all RO_2 react with RO_2, a high-yield reaction or, in the case of isoprene peroxy radical, undergo isomerization to form hydroperoxyenals [HPALDs; *Peeters and Muller*, 2010; *Crounse et al.*, 2011; *Wolfe et al.*, 2012] before yielding CH_2O. These high-yield RO_2 channels increase in importance as NO concentrations decrease (Table 1) and thus buffer α_{eff} to the tenfold decrease of anthropogenic E_{NOx} in background regions (e.g., Ozarks: 0.38 versus $0.39\,P_{CH2O}\,P_{OH}^{-1}$; central Illinois: 0.21 versus $0.24\,P_{CH2O}\,P_{OH}^{-1}$). In cities (e.g., Atlanta: 0.23 versus $0.33\,P_{CH2O}\,P_{OH}^{-1}$), α_{eff} actually increases ~50% for the tenfold reduction of E_{NOx}, in part due to the buffering effects of high-yield RO_2 channels discussed above but also due to a large increase in the yield per RO_2-NO reaction at lower E_{NOx} (0.42 versus $0.52\,P_{CH2O}\,P_{OH}^{-1}$ for high- versus low-E_{NOx} scenarios, respectively; Table 1). The latter effect is likely due to differences of CH_2O yields between the earlier generations and later generations of VOC oxidation caused by the nearly threefold decrease of P_{OH} (Table 1). Thus, we conclude that CH_2O yield from RO_2 chemistry is buffered to the effects of NO_x by high-yield RO_2 channels (Table 1).

OVOC photolysis is a large source of CH_2O in the Ozarks (up to 25%; Table 1). However, more than 90% of the photolytic source of CH_2O over the Ozarks is due to the rapid photolysis of HPALDs ($\tau_{HPALD\text{-}photolysis}$ ~ 30 min). Due to the short lifetime of HPALDs, we attribute its production of CH_2O to its source, the reaction of OH with

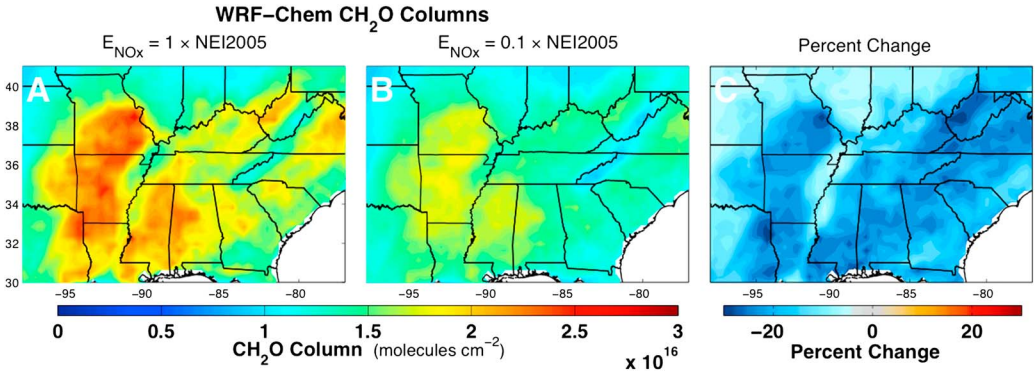

Figure 6. The June–August 2012 average CH_2O column simulated with WRF-Chem at 19 UTC (1 P.M. Central Standard Time; CST), including only cloud-free grid cells over land in (a) the standard simulation, (b) the sensitivity simulation in which anthropogenic E_{NOx} is decreased by a factor of 10, and (c) the percent difference between the two simulations.

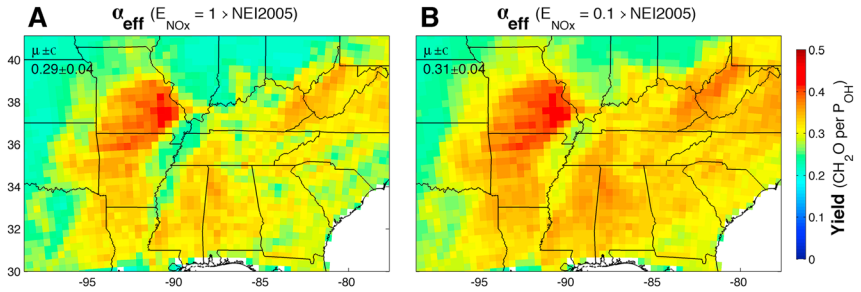

Figure 7. The June–August 2012 1 P.M. CST average of α_{eff} (colors; $P_{CH2O}\,P_{OH}^{-1}$) in the lower troposphere (≲2.5 km) calculated explicitly with WRF-Chem for cloud free grid cells over land in both the (a) standard simulation (E_{NOx} = 1 × NEI2005) and (b) in a simulation with E_{NOx} reduced tenfold (E_{NOx} = 0.1 × NEI2005).

isoprene, thus maintaining our assumption that OVOC photolysis and ozonolysis are relatively small sources of CH_2O in comparison to OH-VOC reactions (Table 1).

3.3.2. Dependence of P_{OH} and VOCR on E_{NOx}

Assuming that α_{eff} does not depend on E_{NOx} (see section 3.3.1), we quantify the response of VOCR, P_{OH} and the CH_2O column to the decrease of anthropogenic E_{NOx} (Figures 5 and 6). In response to the tenfold reduction of E_{NOx}, boundary layer NO_x concentrations decrease 61% and P_{OH} decreases 37%, from 2.7×10^7 molecules $cm^{-3}\,s^{-1}$ (Figure 5a) to 1.7×10^7 molecules $cm^{-3}\,s^{-1}$ (Figure 4b). As a result of the decreased P_{OH}, VOC lifetimes increase and the boundary layer average VOCR increases from 3.1 s^{-1} (Figure 5a) to 4.6 s^{-1} (Figure 5b), much of it due to an increase of isoprene, which increases from a column concentration of 1.2×10^{16} atoms C cm^{-2} to 3.0×10^{16} atoms C cm^{-2}.

The decrease of P_{OH} has both a direct and indirect effect on the CH_2O removal rate due to its feedback on VOCR ($J_{CH2O} + k_{CH2O+OH}\,P_{OH}$/VOCR; equation (1)). In regions where E_{ISOP} is high ($>1\times10^{13}$ molecules $cm^{-2}\,s^{-1}$), we

Table 1. Chemistry Affecting α_{eff} Calculated Instantaneously at 1 P.M. CST for June–August 2012 at High (1×) and Low (0.1×) E_{NOx}

		High VOCR, Low NO_x		High VOCR, High NO_x		Low VOCR, Low NO_x	
		Ozarks, MO		Atlanta, GA		Central, IL	
		37°N, 92°W		34°N, 84°W		40°N, 89°W	
	$E_{NOx\text{-}NEI2005}$	1×	0.1×	1×	0.1×	1×	0.1×
	$[NO]_{PBL}$ (ppt)	33	16	350	54	100	47
Fractional Fate of RO_2	RO_2–NO	0.35	0.22	0.85	0.50	0.60	0.44
	RO_2–HO_2	0.44	0.52	0.11	0.35	0.24	0.35
	RO_2–RO_2	0.14	0.15	0.04	0.12	0.15	0.20
Yield (CH_2O per RO_2 reacted)	Isomerization	0.07	0.11	0.00	0.03	0.00	0.01
	RO_2–NO	0.61	0.63	0.42	0.52	0.53	0.54
	RO_2–HO_2	0.08	0.09	0.01	0.05	0.01	0.02
	RO_2–RO_2	0.49	0.50	0.47	0.48	0.48	0.49
P_{CH2O} by source (×10^6 molecules $cm^{-3}\,s^{-1}$)	RO_2–NO	4.4	2.0	11.4	4.1	4.1	2.2
	RO_2–HO_2	0.8	0.7	0.0	0.3	0.0	0.1
	RO_2–RO_2	1.6	1.2	0.7	1.0	1.0	1.0
	J_{OVOC}	1.6	1.8	0.3	0.7	0.2	0.3
	OH-VOC	0.2	0.2	0.6	0.2	0.5	0.3
	O_3 + alkene	0.9	0.8	0.2	0.3	0.0	0.0
	Total	9.6	6.7	13.4	6.6	5.8	4.0
	P_{OH} (×10^6 molecules $cm^{-3}\,s^{-1}$)	25.2	17.0	57.5	19.8	27.3	16.6
	α_{eff} ($P_{CH2O}\,P_{OH}^{-1}$)	0.38	0.39	0.23	0.33	0.21	0.24
	Fraction of P_{OH} that reacts with VOC or CO (%)	92.8	93.4	83.7	92.3	80.2	84.8

find that P_{OH} decreases 40% and VOCR increases 60% for a combined 62% decrease of the OH concentration (i.e., $\Delta[OH] \sim \Delta P_{OH}/\Delta VOCR$; ~0.6/1.6). However, the net effect on the CH_2O lifetime is much smaller (21% increase) because photolysis does not change (2% difference). Thus, the ~40% reduction in CH_2O production ($\alpha_{eff} P_{OH}$) is offset by a ~ 20% increase in the CH_2O lifetime, half due to the direct impact of declining E_{NOx} on P_{OH} and half due to the indirect feedback on VOCR, resulting in a net 20% decrease of the CH_2O column (Figure 6c). In regions where E_{ISOP} is low, the feedbacks of P_{OH} on the CH_2O lifetime more fully offset its effects on CH_2O production, such that the net effect on the CH_2O column is closer to zero (compare Figures 3a and 6c).

Thus, in response to lower E_{NOx}, the simulated CH_2O column decreases everywhere (Figure 6). The decreases are largest (−23%, Figure 6c) where E_{ISOP} is large ($>10\times10^{12}$ atoms C cm^{-2} s^{-1}) and near zero (−5%) where E_{ISOP} is small ($<1\times10^{12}$ atoms C cm^{-2} s^{-1}), a pattern consistent with a decrease in regional background P_{OH} (Figure 1) and the feedbacks of P_{OH} on CH_2O production and loss described above. Due to larger decreases of the CH_2O column where E_{ISOP} is large, the spatial correlation simulated between the CH_2O column and E_{ISOP} weakens ($r^2 = 0.59$; Figures 3a, and 6b all grid cells; $r^2 = 0.76$, Figures 3a and 6a all grid cells).

We perform the same WRF-Chem simulation with low E_{NOx} (0.1 × NEI2005; Figure 6b) but also decrease E_{ISOP} by 20% over the Ozarks (89.4–94.9°W; 35.3–39.1°N). As expected for low-P_{OH}, high-VOCR conditions (Figure 1), the CH_2O column over the same region is not very sensitive to changes of E_{ISOP} and decreases by only 5.2%. Thus, in this high-VOC regime, a 40% perturbation or bias of P_{OH} can have a twofold larger effect on the CH_2O column (~20%; Figure 6) than does a 20% perturbation of E_{ISOP} (~5%), assuming a linear scaling to compare the perturbations.

3.4. α_{eff}: Dependence on Ambient VOC Mixture

Figure 7 shows the spatial variability of α_{eff} in both the standard and reduced E_{NOx} simulations. The value for α_{eff} ($P_{CH2O}\,P_{OH}^{-1}$) is calculated explicitly from 1 P.M. CST June–August 2012 average values for P_{CH2O} and P_{OH}. The spatial pattern and magnitude of α_{eff} does not depend strongly on the tenfold decrease of E_{NOx} (Figure 7a versus 7b), again demonstrating that α_{eff} is relatively buffered to variations of E_{NOx} (see section 3.3.1). The spatial pattern of α_{eff} in both scenarios reflects differences in the regionally relevant VOC mixture (i.e., isoprene versus background CH_4). In general, α_{eff} is approximately 0.25 $P_{CH2O}\,P_{OH}^{-1}$ in the regional background and is between 0.3 and 0.4 $P_{CH2O}\,P_{OH}^{-1}$ in the high-VOCR regions. Because α_{eff} tends to be large where CH_2O columns are largest and small where CH_2O columns are smallest, the steady state calculation of CH_2O is systematically biased (slope > 1; Figure 4) because it assumes that α_{eff} is spatially constant (α_{eff} =0.30 $P_{CH2O}\,P_{OH}^{-1}$). In background regions, CH_4 ($\alpha_{CH4} \leq 1$) and CO ($\alpha_{CO} = 0$) are the most important sinks of OH. Thus, $\alpha_{eff,background}$ depends on their relative concentration and may change as their abundances change in the future. On the other hand, in isoprene-rich regions, almost every OH radical reacts with isoprene or one of its products, so α_{eff} in these regions will be buffered to any changes in background CO or CH_4 concentrations. Thus, in isoprene-rich regions, long-term trends of the CH_2O column should primarily reflect changing P_{OH} and VOCR assuming that α_{eff} is buffered (see also section 3.3.1).

4. Implications for VOC Emission Inversions From OVOC Measurements

To investigate the implications of our findings for retrieving E_{ISOP} from measurements of the CH_2O column, we evaluate the relationship of the CH_2O column to E_{ISOP} in the WRF-Chem simulation (Figure 8a) and discuss our findings in the context of VOCR (Figure 8b) and the steady state estimate of the CH_2O column (Figure 8c). We average model results (36 km × 36 km) to a coarser spatial scale (216 km × 216 km) similar to the model resolution used in previous analyses [e.g., *Palmer et al*., 2003, 2006; *Millet et al*., 2008; *Barkley et al*., 2008; *Marais et al*., 2012]. We have highlighted values from individual grid cells over the Missouri Ozarks (37°N, 92.5°W; cyan), Alabama (33.5°N, 85.5°W; yellow), and SW Arkansas (33.5°N, 92.5°W; magenta), to illustrate the regional differences among the domain-wide relationships (Figure 8).

As shown previously [e.g., *Palmer et al*., 2003, 2006; *Millet et al*., 2008], there is a strong relationship between the CH_2O column and E_{ISOP} when considering all daily values from individual grid cells as a single statistical ensemble ($r^2 = 0.69$; Figure 8a). As expected for lower P_{OH} conditions, this relationship is weaker in the lower

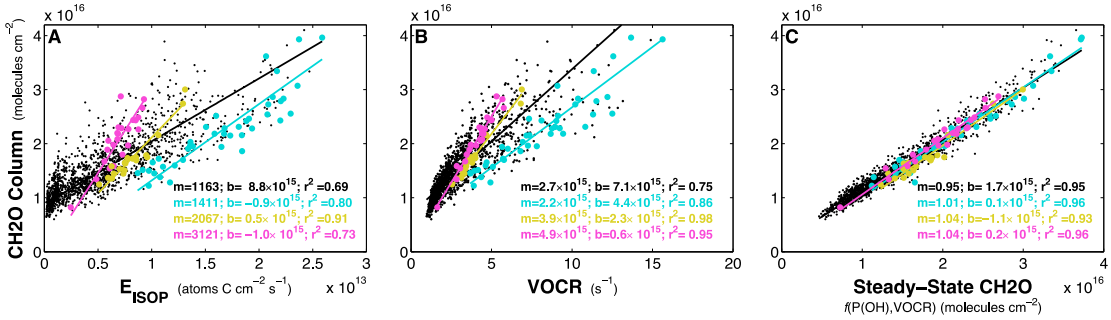

Figure 8. Daily 1 P.M. CH_2O column versus (a) isoprene emissions, (b) VOCR, and (c) the CH_2O column derived by assuming steady state (equation (1); $\alpha_{eff} = 0.3\ P_{CH2O}\ P_{OH}^{-1}$) for June–August 2012 over the southeast U.S. (29°–39°N, 78°–100°W) in the WRF-Chem model. Values are averaged from the native WRF-Chem grid to a coarser grid of 216 km × 216 km. Columns over the Missouri Ozarks (37°N, 92.5°W; cyan), Alabama (33.5°N, 85.5°W; yellow) and SW Arkansas (33.5°N, 92.5°W; magenta) are highlighted to illustrate regional differences in the relationships. Values with cloud fraction above 0.2 are excluded. Reduced major axis least square regression results are reported in the lower right corner.

E_{NOx} simulation ($r^2 = 0.49$). The relationship is varied locally, with inferred slopes varying by more than a factor of 2 between some locations (Figure 8a, colors), confounding the retrieval of E_{ISOP} for a given value of the CH_2O column (e.g., magenta-Ozarks versus cyan-SW Arkansas), a finding also noted in previous studies [e.g., *Millet et al.*, 2008; *Marais et al.*, 2012].

One hypothesis for the regional differences in slopes of CH_2O to E_{ISOP} is that the transport of isoprene and its products from high-emission grid cells to downwind grid cells diminishes the sensitivity of CH_2O to E_{ISOP} in the high-emission grid cells and inflates it downwind [*Millet et al.*, 2008]. However, VOCR accounts for transport, yet its relationship with the CH_2O column is equally varied across the regions (Figures 8a versus 8b; e.g., magenta-Ozarks versus cyan-SW Arkansas), thus excluding transport as the primary cause. The steady state model, on the other hand, is able to explain the regional differences in slopes to within 5% of one another (Figure 8c, colors), suggesting that the regional differences in the relationship of CH_2O to E_{ISOP} or VOCR are due to differences of P_{OH} (Figures 8a and 8b versus Figure 8c).

Despite regional variability, the local relationships of CH_2O to E_{ISOP} or VOCR are remarkably strong, with correlation coefficients ranging from 0.73 to 0.91 for E_{ISOP} (Figure 8a, colors) and from 0.86 to 0.98 for VOCR (Figure 8b, colors). The strong linear relationship between VOCR and CH_2O requires that the other driving variable, P_{OH}, be positively correlated with VOCR such that the day-to-day variation of the OH concentration is small (i.e., daily values of VOCR and P_{OH} lie on a line of constant slope in Figure 1). Positive correlation of VOCR and P_{OH} suggests that the conditions resulting in higher E_{ISOP} and VOCR tend to result in higher P_{OH}: high temperatures and clear skies are associated with larger E_{ISOP} [*Guenther et al.*, 2006], and high concentrations of water vapor and ozone, both of which are important precursors of OH radicals. Assuming that the day-to-day variation of OH is small in any given location, the sensitivity (i.e., slope) of the CH_2O column to a perturbation of VOCR in that location is directly proportional to its OH concentration: the slope is steep where the OH concentration is high (e.g., the rise of CH_2O contours following the gray line with $[OH] = 7 \times 10^6$ molecules cm^{-3} in Figure 1) and is shallow where the OH concentration is low (e.g., the same for the gray line with $[OH] = 3 \times 10^6$ molecules cm^{-3} in Figure 1). This same effect will be weaker for E_{ISOP} due to the feedbacks of P_{OH} on VOCR, but should follow the same general trend (section 3.3.2).

To evaluate this hypothesis, we compare the simulated cloud-free June–August 1 P.M. CST average OH concentration (Figure 9c) to the CH_2O column sensitivity to VOCR (Figure 9b) and E_{ISOP} (Figure 9a) at the native model resolution (36×36 km^2). As expected based on Figure 1, the concentration of OH explains much of the spatial variance of the CH_2O column sensitivity to VOCR ($r^2 = 0.64$; Figures 9b versus 9c). The CH_2O lifetime at 1 P.M. is too short (~2 h) for its transport to strongly influence its relationship with VOCR downwind. Furthermore, any transport will similarly affect VOCR, thus not disturbing their ratio.

Performing the same analysis for E_{ISOP} instead of VOCR, we find that the quantitative agreement is not as strong ($r^2 = 0.26$; Figures 9a versus 9c), but qualitatively, the results are similar. Previous analyses found anomalously high sensitivities in grid cells where summer average E_{ISOP} was low, attributing the enhancement to transport from

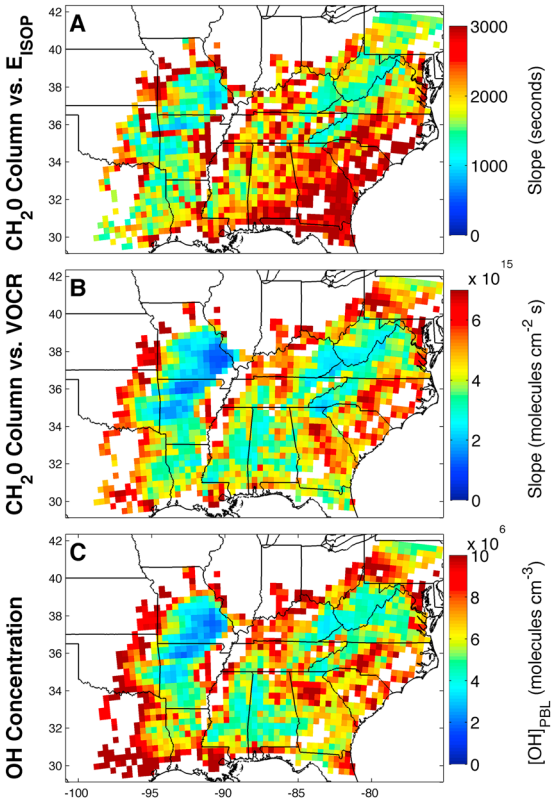

Figure 9. The scaling factor relating CH_2O columns to (a) E_{ISOP} (seconds) and (b) VOCR (molecule cm^{-2} s) derived as the slope from reduced major axis linear regression within each individual WRF-Chem grid cell over land where June–August 2012 average $E_{ISOP} > 5 \times 10^{12}$ atom C cm^{-2} s^{-1}, screened for cloud-free conditions. Also shown is (c) the June–August 2012 boundary layer average OH concentration (molecules cm^{-3}) in grid cells meeting these criteria.

larger upwind sources ($<2 \times 10^{12}$ atom C cm^{-2} s^{-1}) [*Millet et al.*, 2008]. We restrict our analysis to grid cells where average E_{ISOP} is greater than 5×10^{12} atom C cm^{-2} s^{-1}. Transport of isoprene and its oxidation products does affect the sensitivity (slope) of CH_2O to E_{ISOP} at the edge of large isoprene sources (e.g., Figure 9a, downwind edge of the Ozarks) [e.g., *Millet et al.*, 2008], but the spatial pattern of OH concentrations also plays a role (Figure 9c). CH_2O columns are most sensitive to E_{ISOP} over cities where OH concentrations are highest and are less sensitive in regions where E_{ISOP} is largest and OH concentrations are lowest (Figures 3a and 9). We would not expect the relationship between OH concentrations and the CH_2O-to-E_{ISOP} slopes (Figures 9a versus 9c) to be as strong as that for VOCR (Figures 9b versus 9c) because of VOC transport [e.g., *Millet et al.*, 2008], particularly at this finer spatial scale and in light of feedbacks of OH concentrations on VOCR [e.g., *Karl et al.*, 2009, section 3.3.2].

The slopes and *y* intercepts inferred for regressions of the CH_2O column to variations of E_{ISOP} depend on the temporal and spatial scale over which they are derived and thus should not be applied to other temporal and spatial scales (Figures 3, 6, 8, and 9). For example, the slope retrieved for the entire ensemble of grid cells is smaller than the slope derived in every individual grid cell (Figure 8a), a gross bias due to combining high E_{ISOP}, low-OH locations (i.e., the Ozarks) with lower E_{ISOP}, higher-OH locations. The range of the locally derived *y* intercepts in the same example is also large (Figure 8a; $\mu \pm \sigma$; $0.1 \times 10^{15} \pm 3.0 \times 10^{15}$ molecules cm^{-2}) and their average is much smaller than the *y* intercept derived for the entire ensemble of grid cells (Figure 8a; 8.8×10^{15} molecules cm^{-2}). Thus, the *y* intercept does not only represent the background CH_2O column in the absence of isoprene emission [e.g., *Palmer et al.*, 2006] but also reflects nonlinearities in the OH and VOC chemistry that drive CH_2O variability (Figures 1 and 5). As such, the *y* intercept should be treated as a free variable along with the scaling parameter (slope).

Based on our findings, we recommend a full formal inversion to derive E_{ISOP} from measurements of the CH_2O column that accounts for nonlinearities of the OH and VOC chemistry. However, as long as the day-to-day variability of OH concentrations under cloud free conditions is small (Figure 1; lines of constant slope), our results provide a basis (Figure 9) for performing inversions using locally derived linear formulations, originally introduced by *Millet et al.* [2008] and improved by *Marais et al.* [2012]. These inversions should account for spatial variations of the OH concentration and recognize the limitations of inferring variations of E_{ISOP} in low-P_{OH} environments (e.g., Figure 6b). *Marais et al.* [2012] incorporated information on the variability of the NO_2 column, an adaptation that implicitly accounts for some, but not all of the variability of OH concentrations, and is also uncertain in regions where NO_2 columns are near their detection limit. We recommend that a first test of any linear inversion is the comparison of a second iteration of the updated forward model with the CH_2O column measurements.

The influence of OH on the variability of CH_2O is due to the short photolytic lifetime of CH_2O relative to that of reaction with OH (see equation (1)). Thus, the findings that we present here, that variations of the OH radical

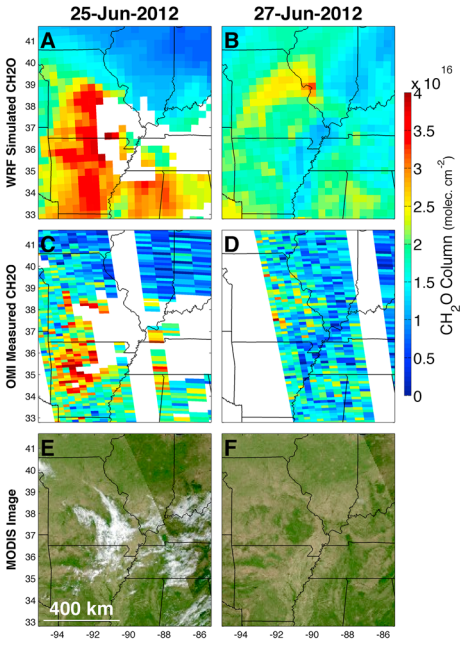

Figure 10. WRF-Chem (a and b) and OMI measurements (c and d) of the CH_2O column at 1 P.M. CST on a day when (Figures 10a, 10c, and 10e) P_{OH} is high (25 June 2012) and on a day when (Figures 10b, 10d, and 10f) P_{OH} is low (27 June 2012). E_{ISOP} varied little between these 2 days over the central U.S. (~3% decrease simulated using WRF-Chem/MEGANv2.04). The OMI view geometry is similar on both days (~200 km further east on 27 June 2012). MODIS true color composite images (e and f) recorded ~15 min prior to the OMI measurements indicate areas of vegetation and the cloud distribution.

influence the variability of CH_2O, also apply to other oxidized VOC intermediates with short lifetimes against photolysis (e.g., glyoxal; $\tau_{photolysis} \sim 2$ h; $\tau_{OH+glyoxal} \sim 2.8$ h at $[OH] = 1 \times 10^7$ molecules cm^{-2}).

5. Daily Variations of the CH_2O Column

The daily variability of CH_2O column has been used to infer daily variability of E_{ISOP} [e.g., *Palmer et al.*, 2003]. However, the factors affecting P_{OH} and thus its influence on the CH_2O column also vary daily. From 25 June 2012 to 27 June 2012 (Figures 3b, 3c, 3e, 3f, 3h, 3i, 3k, 3l, 3n, and 3o), boundary layer average P_{OH} decreases from 4.2×10^7 molecules cm^{-3} s^{-1} to 2.4×10^7 molecules cm^{-3} s^{-1} over Arkansas and Missouri, two U.S. states in the center west of the domain. The decrease of P_{OH} is due primarily to a decrease of water vapor in the region (i.e., less $O^1D + H_2O \rightarrow 2$ OH). The MODIS near infrared retrieval of the water vapor column indicates that WRF is accurately simulating the regional-scale patterns of the observed water vapor distribution (not shown). On these same days, there is little change in E_{ISOP} (~3%, 1.13×10^{13} to 1.10×10^{13} atoms C cm^{-2} s^{-1}), VOCR (~5%, 5.8 s^{-1} versus 5.5 s^{-1}) or ground-level temperature (33.5°C versus 32.5°C) over the region. Due to the low-P_{OH}, high-VOCR conditions, the CH_2O column in the region is sensitive to the decrease of P_{OH} (Figure 1) and the statewide average CH_2O column over Missouri and Arkansas decreases from 2.6×10^{16} molecules cm^{-2} on 25 June 2012 to 1.9×10^{16} molecules cm^{-2} on 27 June 2012, a decrease that is well explained by the steady state model (Figures 3k, 3l, 3n, and 3o). This result again highlights the need to use the appropriate time and space domains for any inversion of E_{ISOP} from measurements of the CH_2O column, as the sensitivity of the CH_2O column to E_{ISOP} depends on daily variations of P_{OH}.

To demonstrate that these daily variations of the CH_2O column are observable, Figure 10 shows the CH_2O columns measured by the Ozone Monitoring Instrument (OMI) from the most recent NASA/SAO product (version 3) [*González Abad et al.*, 2015] and again shows those simulated by WRF-Chem (see also Figure 3), zoomed in over the south-central U.S. on 25 and 27 June 2012. The spatial pattern of the simulated CH_2O column matches the observations at a regional scale (Figure 10). On 25 June 2012, the CH_2O columns are minimum in the northeast corner of the domain but larger throughout the rest of the domain, even exceeding 4×10^{16} molecules cm^{-2} in north central Arkansas, an indication that boundary layer average P_{OH} ($>4 \times 10^7$ molecules cm^{-3} s^{-1}) and VOCR (>7.5 s^{-1}) are both high (i.e., toward the upper right corner of Figure 1). On 27 June 2012, the columns are much lower throughout the domain with a local minimum in the center of the image and in the far northeast corner, indicating that either P_{OH} or VOCR is lower than it was on 25 June 2012. Canopy-scale isoprene flux measurements in the region increased from 25 June to 27 June 2012 [*Seco et al.*, 2015] (38.74°N, 92.20°W) suggesting that VOCR is unlikely to be lower on 27 June. Consequently, the observed decrease in the CH_2O columns is likely due to the decrease of P_{OH} in the region (Figures 3h and 3i), primarily driven by the decrease of water vapor.

The simulated CH_2O columns are biased high relative to the measurements on both days (Figure 10), suggesting that the simulated P_{OH} or VOCR is biased high, though it is also possible that the measurements are systematically biased. If the air mass factor (AMF) from version 2 of the retrieval were applied to the

version 3 slant columns, the vertical columns would be approximately 33% larger, and in better agreement with the simulated values. We are not suggesting that the AMF from one version is better than the other but are rather highlighting the systematic uncertainty of the measurements due to retrieval inputs [e.g., *Palmer et al*., 2001; *Russell et al*., 2011; *Barkley et al*., 2012].

6. Variability of the CH_2O Column: A Constraint on P_{OH}?

Despite these potential biases, the observed variability suggests that in addition to reflecting variations of isoprene emissions due to temperature [e.g., *Palmer et al*., 2003], the CH_2O column reflects variation of OH sources, such as ozone, NO_x, water vapor and of particular interest, the magnitude of a potentially large hypothesized source of OH in high-VOC, low-NO_x environments [*Lelieveld et al*., 2008; *Hofzumahaus et al*., 2009; *Whalley et al*., 2011; *Mao et al*., 2012; *Taraborrelli et al*., 2012; *Fuchs et al*., 2013; *Nolscher et al*., 2014; *Rohrer et al*., 2014]. Measurement-based studies suggest that our conventional understanding of OH sources grossly underestimates P_{OH} in high-isoprene, low-NO_x conditions (e.g., $1\times-3\times$ conventional sources) [*Lelieveld et al*., 2008; *Fuchs et al*., 2013], However, there is also evidence from quantitative, detailed laboratory studies [*Paulot et al*., 2009a, 2009b; *Crounse et al*., 2011, 2012] and the field [e.g., *Mao et al*., 2012] that suggests that the magnitude of the postulated OH sources is not much larger than conventionally understood.

If the postulated source of OH were much larger than what is conventionally understood ($1\times-3\times$ conventional sources) [e.g., *Lelieveld et al*., 2008; *Fuchs et al*., 2013], then the CH_2O column should be less sensitive to variations of P_{OH} and more sensitive to variations of VOCR (i.e., toward the top of Figure 1; $[OH]\geq 5\times10^6$ molecules cm^{-3}). However, the observations show that the CH_2O column is sensitive to the variability of conventional sources of OH (i.e., water vapor). The observed variability (Figure 10) is in line with that simulated in WRF-Chem, which we estimate regenerates approximately 33% of conventional OH sources in isoprene-rich conditions [e.g., *Paulot et al*., 2009a, 2009b; *Crounse et al*., 2011, 2012], approximately an order of magnitude less than that postulated based on recent OH measurements (~threefold increase) [e.g., *Lelieveld et al*., 2008], To make this estimate, we classify OH production in to five classes and assume that all production via photolysis, RO_2-HO_2 and VOC-OH reactions are unconventional while that due to inorganic reactions and ozonolysis is conventional and is thus an upper bound on the estimated rate. We isolate the effect of low-NO_x isoprene chemistry by making the estimate for 27 June 2012 over the Ozarks (37.4°N, 91.1°W), where surface level isoprene concentrations are high (18 ppb) and NO concentrations are low (47 parts per trillion (ppt)).

Thus, the observed variability is consistent with an OH source with a magnitude that is closer to that of conventional sources (i.e., toward the bottom of Figure 1). The large uncertainty of any single column measurement [e.g., *González Abad et al*., 2015] limits the strength with which we can make this conclusion from only two overpasses (25 and 27 June 2012; Figure 10). However, in situ measurements of CH_2O also indicate that a source of OH far larger than conventionally understood is not consistent with the observed abundance of CH_2O [e.g., *Butler et al*., 2008; *Galloway et al*., 2012].

7. Conclusions

We describe the variability of the fully simulated June–August 1 P.M. CST CH_2O column in WRF-Chem (Figures 2–9) using a steady state framework (equation (1) and Figures 1 and 6) with simulated P_{OH} and VOCR as the only variables. We find that the CH_2O column depends on P_{OH} most strongly where the midday OH concentration is low and depends on VOCR where the midday OH concentration is high (Figure 1). We find that the spatial pattern of E_{ISOP} in the east U.S. drives the pattern of VOCR (Figure 3). Thus, based on the spatial pattern of the OH concentration simulated in WRF-Chem (~ P_{OH}/VOCR; Figure 9c), we conclude that the CH_2O column is most sensitive to E_{ISOP} where E_{ISOP} is small or where P_{OH} is large and is least sensitive to E_{ISOP} where E_{ISOP} is large (Figures 9a versus 9c). The opposite is true for the relationship of P_{OH} to the CH_2O column.

Our findings indicate that variability of the OH concentration should be considered when using measurements of the CH_2O column to understand the variability of E_{ISOP} and other VOC emissions. Our finding has been alluded to in previous work [e.g., *Marais et al*., 2012] but was not attributed to the variability of P_{OH}. The prior attribution to NO_x [*Marais et al*., 2012] is consistent with our findings in that NO_x is a large source

of OH radicals but neglects the impacts of other OH sources such as water vapor, ozone, or possible isoprene-dependent OH production pathways recently discovered [*Crounse et al*., 2011, 2012] or hypothesized [e.g., *Lelieveld et al*., 2008; *Hofzumahaus et al*., 2009]. We examine the influence of NO_x on RO_2 chemistry by tracking the CH_2O yield from individual radical reaction pathways and find that the yield of CH_2O at low NO_x concentrations is buffered by high-yield RO_2-RO_2 reactions (Table 1). Thus, we conclude that in isoprene-rich regions, the influence of NO_x on CH_2O production is primarily due to its feedback on P_{OH}, which controls the rate of RO_2 formation and less so through its effect on the fate of individual RO_2.

Our findings suggest that measurements of the CH_2O column have the potential to improve our understanding of OH chemistry. For example, our framework (Figure 1) implies that measurements of the CH_2O column in regions where VOCR is known to be high [e.g., *Lelieveld et al*., 2008] (~10 s^{-1}) [*Hofzumahaus et al*., 2009] (~ 20 s^{-1}) can be used to test hypothesized OH sources, insofar as the assumption of a relatively insensitive CH_2O yield per P_{OH} (α_{eff}) is valid for any changes to the oxidation mechanism. While this assumption would not hold for all possible isoprene oxidation mechanisms or VOC environments, we show here that the yield of CH_2O per P_{OH} (α_{eff}) in a state-of-the-science chemical mechanism is insensitive to a broad range of photochemical conditions in an isoprene-rich environment (Figure 7; Table 1). Regardless of these details, any proposed isoprene oxidation mechanism must reconcile itself with CH_2O measurements (as well as those of other oxidized VOC), a task which has proven difficult in previous modeling analyses [e.g., *Butler et al*., 2008; *Galloway et al*., 2012].

Acknowledgments

This work was supported by the NOAA Climate and Global Change Fellowship Program (http://www.vsp.ucar.edu/cgc/) and by the NASA Air Quality Applied Sciences Team (NNX12AF15G). We thank two anonymous reviewers and Bryan Duncan for their thoughtful and helpful comments. We acknowledge Eleanor Browne and Wendy Goliff for use of the RACM2 chemical mechanism with updates to isoprene and monoterpene nitrate chemistry [*Browne et al*., 2014]. We acknowledge the use of the WRF-Chem model Version 3.5.1 made available at http://www2.mmm.ucar.edu/wrf/users/download/get_source.html. Model results and tools used to generate production and loss rates in WRF-Chem will be made available upon request to the corresponding author. We acknowledge the use of OMI/Aura Formaldehyde (HCHO) Total Column 1-orbit L2 Swath 13 × 24 km (V003) available at http://disc.sci.gsfc.nasa.gov/Aura/data-holdings/OMI/omhcho_v003.shtml. We acknowledge the Atmospheric Chemistry Working Group of the WRF model for providing the ftp://aftp.fsl.noaa.gov/divisions/taq/emissions_-data_2005/. We acknowledge the use of MOZART-4 global model output and the use of the WRF-Chem preprocessor tools (mozbc and bioemiss) both made available at https://www2.acom.ucar.edu/wrf-chem/wrf-chem-tools-community provided by the Atmospheric Chemistry Observations and Modeling Lab (ACOM) of NCAR.

References

Abbot, D. S., P. I. Palmer, R. V. Martin, K. V. Chance, D. J. Jacob, and A. Guenther (2003), Seasonal and interannual variability of North American isoprene emissions as determined by formaldehyde column measurements from space, *Geophys. Res. Lett.*, *30*(17), 1886, doi:10.1029/2003GL017336.

Archibald, A. T., M. C. Cooke, S. R. Utembe, D. E. Shallcross, R. G. Derwent, and M. E. Jenkin (2010), Impacts of mechanistic changes on HO_x formation and recycling in the oxidation of isoprene, *Atmos. Chem. Phys.*, *10*(17), 8097–8118.

Barkley, M. P., P. I. Palmer, U. Kuhn, J. Kesselmeier, K. Chance, T. P. Kurosu, R. V. Martin, D. Helmig, and A. Guenther (2008), Net ecosystem fluxes of isoprene over tropical South America inferred from Global Ozone Monitoring Experiment (GOME) observations of HCHO columns, *J. Geophys. Res.*, *113*, D20304, doi:10.1029/2008JD009863.

Barkley, M. P., T. P. Kurosu, K. Chance, I. De Smedt, M. Van Roozendael, A. Arneth, D. Hagberg, and A. Guenther (2012), Assessing sources of uncertainty in formaldehyde air mass factors over tropical South America: Implications for top-down isoprene emission estimates, *J. Geophys. Res.*, *117*, D13304, doi:10.1029/2011JD016827.

Barkley, M. P., et al. (2013), Top-down isoprene emissions over tropical South America inferred from SCIAMACHY and OMI formaldehyde columns, *J. Geophys. Res. Atmos.*, *118*, 6849–6868, doi:10.1002/jgrd.50552.

Boeke, N. L., et al. (2011), Formaldehyde columns from the Ozone Monitoring Instrument: Urban versus background levels and evaluation using aircraft data and a global model, *J. Geophys. Res.*, *116*, D05303, doi:10.1029/2010JD014870.

Browne, E. C., P. J. Wooldridge, K. E. Min, and R. C. Cohen (2014), On the role of monoterpene chemistry in the remote continental boundary layer, *Atmos. Chem. Phys.*, *14*(3), 1225–1238.

Butler, T. M., D. Taraborrelli, C. B. H. Fischer, H. Harder, M. Martinez, J. Williams, M. G. Lawrence, and J. Lelieveld (2008), Improved simulation of isoprene oxidation chemistry with the ECHAM5/MESSy chemistry-climate model: Lessons from the GABRIEL airborne field campaign, *Atmos. Chem. Phys.*, *8*(16), 4529–4546.

Carlton, A. G., and K. R. Baker (2011), Photochemical Modeling of the Ozark Isoprene Volcano: MEGAN, BEIS, and Their Impacts on Air Quality Predictions, *Environ. Sci. Technol.*, *45*(10), 4438–4445.

Chance, K., X. Liu, R. M. Suleiman, D. E. Flittner, J. Al-Saadi, and S. J. Janz (2013), Tropospheric emissions: Monitoring of pollution (TEMPO), Conference on Earth Observing Systems XVIII, San Diego, Calif.

Crounse, J. D., F. Paulot, H. G. Kjaergaard, and P. O. Wennberg (2011), Peroxy radical isomerization in the oxidation of isoprene, *Phys. Chem. Chem. Phys.*, *13*(30), 13,607–13,613.

Crounse, J. D., H. C. Knap, K. B. Ornso, S. Jorgensen, F. Paulot, H. G. Kjaergaard, and P. O. Wennberg (2012), Atmospheric Fate of Methacrolein: 1. Peroxy Radical Isomerization Following Addition of OH and O-2, *J. Phys. Chem. A*, *116*(24), 5756–5762.

Curci, G., P. I. Palmer, T. P. Kurosu, K. Chance, and G. Visconti (2010), Estimating European volatile organic compound emissions using satellite observations of formaldehyde from the Ozone Monitoring Instrument, *Atmos. Chem. Phys.*, *10*(23), 11,501–11,517.

De Smedt, I., T. Stavrakou, J. F. Muller, R. J. van der A, and M. Van Roozendael (2010), Trend detection in satellite observations of formaldehyde tropospheric columns, *Geophys. Res. Lett.*, *37*, L18808, doi:10.1029/2010GL044245.

De Smedt, I., M. Van Roozendael, T. Stavrakou, J. F. Muller, C. Lerot, N. Theys, P. Valks, N. Hao, and R. van der A (2012), Improved retrieval of global tropospheric formaldehyde columns from GOME-2/MetOp-A addressing noise reduction and instrumental degradation issues, *Atmos. Meas. Tech.*, *5*(11), 2933–2949.

Dee, D., et al. (2011), The ERA-Interim reanalysis: Configuration and performance of the data assimilation system, *Q. J. R. Meteorol. Soc.*, *137*(656), 553–597.

Dufour, G., F. Wittrock, M. Camredon, M. Beekmann, A. Richter, B. Aumont, and J. P. Burrows (2009), SCIAMACHY formaldehyde observations: Constraint for isoprene emission estimates over Europe?, *Atmos. Chem. Phys.*, *9*(5), 1647–1664.

Duncan, B. N., et al. (2010), Application of OMI observations to a space-based indicator of NOx and VOC controls on surface ozone formation, *Atmos. Environ.*, *44*(18), 2213–2223.

Emmons, L. K., et al. (2010), Description and evaluation of the Model for Ozone and Related chemical Tracers, version 4 (MOZART-4), *Geosci. Model Dev.*, *3*(1), 43–67.

Fishman, J., et al. (2012), The United States' next generation of atmospheric composition and coastal ecosystem measurements—NASA's Geostationary Coastal and Air Pollution Events (GEO-CAPE) Mission, *Bull. Am. Meteorol. Soc.*, *93*(10), 1547–1566.

Fortems-Cheiney, A., F. Chevallier, I. Pison, P. Bousquet, M. Saunois, S. Szopa, C. Cressot, T. P. Kurosu, K. Chance, and A. Fried (2012), The formaldehyde budget as seen by a global-scale multi-constraint and multi-species inversion system, *Atmos. Chem. Phys.*, *12*(15), 6699–6721.

Fu, T.-M., D. J. Jacob, P. I. Palmer, K. Chance, Y. X. Wang, B. Barletta, D. R. Blake, J. C. Stanton, and M. J. Pilling (2007), Space-based formaldehyde measurements as constraints on volatile organic compound emissions in east and south Asia and implications for ozone, *J. Geophys. Res.*, *112*, D06312, doi:10.1029/2006JD007853.

Fuchs, H., et al. (2013), Experimental evidence for efficient hydroxyl radical regeneration in isoprene oxidation, *Nat. Geosci.*, *6*(12), 1023–1026.

Galloway, M. M., et al. (2012), Observations and modeling of formaldehyde at the PROPHET mixed hardwood forest site in 2008, *Atmos. Environ.*, *49*, 403–410.

Goliff, W. S., W. R. Stockwell, and C. V. Lawson (2013), The regional atmospheric chemistry mechanism, version 2, *Atmos. Environ.*, *68*, 174–185.

González Abad, G., X. Liu, K. Chance, H. Wang, T. P. Kurosu, and R. Suleiman (2015), Updated Smithsonian Astrophysical Observatory Ozone Monitoring Instrument (SAO OMI) formaldehyde retrieval, *Atmos. Meas. Tech.*, *8*(1), 19–32.

Grell, G. A., S. E. Peckham, R. Schmitz, S. A. McKeen, G. Frost, W. C. Skamarock, and B. Eder (2005), Fully coupled "online" chemistry within the WRF model, *Atmos. Environ.*, *39*(37), 6957–6975.

Guenther, A., T. Karl, P. Harley, C. Wiedinmyer, P. I. Palmer, and C. Geron (2006), Estimates of global terrestrial isoprene emissions using MEGAN (Model of Emissions of Gases and Aerosols from Nature), *Atmos. Chem. Phys.*, *6*, 3181–3210.

Hofzumahaus, A., et al. (2009), Amplified trace gas removal in the troposphere, *Science*, *324*(5935), 1702–1704.

Jin, X., and T. Holloway (2015), Spatial and temporal variability of ozone sensitivity over China observed from the Ozone Monitoring Instrument, *J. Geophys. Res. Atmos.*, 7229–7246, doi:10.1002/2015JD023250.

Karl, T., A. Guenther, A. Turnipseed, G. Tyndall, P. Artaxo, and S. Martin (2009), Rapid formation of isoprene photo-oxidation products observed in Amazonia, *Atmos. Chem. Phys.*, *9*(20), 7753–7767.

Lamsal, L. N., B. N. Duncan, Y. Yoshida, N. A. Krotkov, K. E. Pickering, D. G. Streets, and Z. Lu (2015), U.S. NO2 trends (2005-2013): EPA Air Quality System (AQS) data versus improved observations from the Ozone Monitoring Instrument (OMI), *Atmos. Environ.*, *110*, 130–143.

Lelieveld, J., et al. (2008), Atmospheric oxidation capacity sustained by a tropical forest, *Nature*, *452*(7188), 737–740.

Mao, J., et al. (2012), Insights into hydroxyl measurements and atmospheric oxidation in a California forest, *Atmos. Chem. Phys.*, *12*(17), 8009–8020.

Mao, J., F. Paulot, D. J. Jacob, R. C. Cohen, J. D. Crounse, P. O. Wennberg, C. A. Keller, R. C. Hudman, M. P. Barkley, and L. W. Horowitz (2013), Ozone and organic nitrates over the eastern United States: Sensitivity to isoprene chemistry, *J. Geophys. Res. Atmos.*, *118*, 11,256–11,268, doi:10.1002/jgrd.50817.

Marais, E. A., et al. (2012), Isoprene emissions in Africa inferred from OMI observations of formaldehyde columns, *Atmos. Chem. Phys.*, *12*(14), 6219–6235.

Marais, E. A., D. J. Jacob, A. Guenther, K. Chance, T. P. Kurosu, J. G. Murphy, C. E. Reeves, and H. O. T. Pye (2014), Improved model of isoprene emissions in Africa using Ozone Monitoring Instrument (OMI) satellite observations of formaldehyde: Implications for oxidants and particulate matter, *Atmos. Chem. Phys.*, *14*(15), 7693–7703.

Martin, R. V., A. M. Fiore, and A. Van Donkelaar (2004), Space-based diagnosis of surface ozone sensitivity to anthropogenic emissions, *Geophys. Res. Lett.*, *31*, L06120, doi:10.1029/2004GL019416.

Millet, D. B., D. J. Jacob, K. F. Boersma, T. M. Fu, T. P. Kurosu, K. Chance, C. L. Heald, and A. Guenther (2008), Spatial distribution of isoprene emissions from North America derived from formaldehyde column measurements by the OMI satellite sensor, *J. Geophys. Res.*, *113*, D02307, doi:10.1029/2007JD008950.

Nolscher, A. C., T. Butler, J. Auld, P. Veres, A. Munoz, D. Taraborrelli, L. Vereecken, J. Lelieveld, and J. Williams (2014), Using total OH reactivity to assess isoprene photooxidation via measurement and model, *Atmos. Environ.*, *89*, 453–463.

Palmer, P. I., D. J. Jacob, K. Chance, R. V. Martin, R. J. D. Spurr, T. P. Kurosu, I. Bey, R. Yantosca, A. Fiore, and Q. B. Li (2001), Air mass factor formulation for spectroscopic measurements from satellites: Application to formaldehyde retrievals from the Global Ozone Monitoring Experiment, *J. Geophys. Res.*, *106*(D13), 14,539–14,550, doi:10.1029/2000JD900772.

Palmer, P. I., D. J. Jacob, A. M. Fiore, R. V. Martin, K. Chance, and T. P. Kurosu (2003), Mapping isoprene emissions over North America using formaldehyde column observations from space, *J. Geophys. Res.*, *108*(D6), 4180, doi:10.1029/2002JD002153.

Palmer, P. I., et al. (2006), Quantifying the seasonal and interannual variability of North American isoprene emissions using satellite observations of the formaldehyde column, *J. Geophys. Res.*, *111*, D12315, doi:10.1029/2005JD006689.

Paulot, F., J. D. Crounse, H. G. Kjaergaard, J. H. Kroll, J. H. Seinfeld, and P. O. Wennberg (2009a), Isoprene photooxidation: New insights into the production of acids and organic nitrates, *Atmos. Chem. Phys.*, *9*(4), 1479–1501.

Paulot, F., J. D. Crounse, H. G. Kjaergaard, A. Kuerten, J. M. S. Clair, J. H. Seinfeld, and P. O. Wennberg (2009b), Unexpected epoxide formation in the gas-phase photooxidation of isoprene, *Science*, *325*(5941), 730–733.

Peeters, J., and J.-F. Muller (2010), HOx radical regeneration in isoprene oxidation via peroxy radical isomerisations. II: Experimental evidence and global impact, *Phys. Chem. Chem. Phys.*, *12*(42), 14,227–14,235.

Rohrer, F., et al. (2014), Maximum efficiency in the hydroxyl-radical-based self-cleansing of the troposphere, *Nat. Geosci.*, *7*(8), 559–563.

Russell, A. R., A. E. Perring, L. C. Valin, E. J. Bucsela, E. C. Browne, K. E. Min, P. J. Wooldridge, and R. C. Cohen (2011), A high spatial resolution retrieval of NO_2 column densities from OMI: Method and evaluation, *Atmos. Chem. Phys.*, *11*(16), 8543–8554.

Russell, A. R., L. C. Valin, and R. C. Cohen (2012), Trends in OMI NO2 observations over the United States: Effects of emission control technology and the economic recession, *Atmos. Chem. Phys.*, *12*(24), 12,197–12,209.

Seco, R., T. Karl, A. Guenther, K. P. Hosman, S. G. Pallardy, L. H. Gu, C. Geron, P. Harley, and S. Kim (2015), Ecosystem-scale volatile organic compound fluxes during an extreme drought in a broadleaf temperate forest of the Missouri Ozarks (central USA), *Global Change Biol.*, *21*(10), 3657–3674.

Song, C. H., H. S. Kim, R. von Glasow, P. Brimblecombe, J. Kim, R. J. Park, J. H. Woo, and Y. H. Kim (2010), Source identification and budget analysis on elevated levels of formaldehyde within the ship plumes: A ship-plume photochemical/dynamic model analysis, *Atmos. Chem. Phys.*, *10*(23), 11,969–11,985.

Stavrakou, T., J. F. Mueller, I. De Smedt, M. Van Roozendael, G. R. van der Werf, L. Giglio, and A. Guenther (2009a), Global emissions of non-methane hydrocarbons deduced from SCIAMACHY formaldehyde columns through 2003–2006, *Atmos. Chem. Phys.*, *9*(11), 3663–3679.

Stavrakou, T., J. F. Muller, I. De Smedt, M. Van Roozendael, G. R. van der Werf, L. Giglio, and A. Guenther (2009b), Evaluating the performance of pyrogenic and biogenic emission inventories against one decade of space-based formaldehyde columns, *Atmos. Chem. Phys.*, *9*(3), 1037–1060.

Sumner, A. L., et al. (2001), A study of formaldehyde chemistry above a forest canopy, *J. Geophys. Res.*, *106*(D20), 24,387–24,405, doi:10.1029/2000JD900761.

Taraborrelli, D., M. G. Lawrence, J. N. Crowley, T. J. Dillon, S. Gromov, C. B. M. Gross, L. Vereecken, and J. Lelieveld (2012), Hydroxyl radical buffered by isoprene oxidation over tropical forests, *Nat. Geosci.*, *5*(3), 190–193.

Whalley, L. K., et al. (2011), Quantifying the magnitude of a missing hydroxyl radical source in a tropical rainforest, *Atmos. Chem. Phys.*, *11*(14), 7223–7233.

Wiedinmyer, C., et al. (2005), Ozarks Isoprene Experiment (OZIE): Measurements and modeling of the "isoprene volcano", *J. Geophys. Res.*, *110*, D18307, doi:10.1029/2005JD005800.

Witte, J. C., B. N. Duncan, A. R. Douglass, T. P. Kurosu, K. Chance, and C. Retscher (2011), The unique OMI HCHO/NO2 feature during the 2008 Beijing Olympics: Implications for ozone production sensitivity, *Atmos. Environ.*, *45*(18), 3103–3111.

Wolfe, G. M., J. D. Crounse, J. D. Parrish, J. M. St. Clair, M. R. Beaver, F. Paulot, T. P. Yoon, P. O. Wennberg, and F. N. Keutsch (2012), Photolysis, OH reactivity and ozone reactivity of a proxy for isoprene-derived hydroperoxyenals (HPALDs), *Phys. Chem. Chem. Phys.*, *14*(20), 7276–7286.

Zhu, L., D. J. Jacob, L. J. Mickley, E. A. Marais, D. S. Cohan, Y. Yoshida, B. N. Duncan, G. G. Abad, and K. V. Chance (2014), Anthropogenic emissions of highly reactive volatile organic compounds in eastern Texas inferred from oversampling of satellite (OMI) measurements of HCHO columns, *Environ. Res. Lett.*, *9*(11), doi:10.1088/1748-9326/9/11/114004.